Open Archive Toulouse Archive Ouverte (OATAO)

This is an author's version published in: https://oatao.univ-toulouse.fr/18406

Official URL : https://doi.org/10.1016/j.compstruct.2017.07.080

To cite this version :

Validation and modeling of aeronautical composite structures subjected to combined loadings: The VERTEX project. Part 1: Experimental setup, FE-DIC instrumentation and procedures

Joël Serra, J.E. Pierré, J.C. Passieux, J.N. Périé, Christophe Bouvet, Bruno Castanié [*]

Institut Clément Ader (ICA), Université de Toulouse, CNRS UMR 5312-INSA-ISAE Supaéro-Mines Albi-UPS, Toulouse, France

ABSTRACT

The development and certification of aeronautical composite structures is still largely based on the pyramid of tests. This approach is extremely costly in terms of number of tests and design loops. Moreover, it is based on uniaxial tests whereas the real structures are mostly subjected to combined loadings. The aim of the collaborative research program "VERTEX" is to progress towards Predictive Virtual Testing and to significantly reduce the development costs of aeronautical and space programs. In this first part, the specific methodology for multiaxial tests of aeronautical structures is presented. The concept of the technological specimen and its size are justified. Then, the development of a specific test rig is presented, on which compression/tension, shear, internal pressure and combinations are possible. Since structural tests are complex to instrument, a specific full-field measurement technique is developed. It is based on a multi-camera instrumentation and an original Finite Element approach to Stereo Digital Image Correlation (FE-SDIC). Within such a framework, given that the very same mesh can be used for the simulation and the measurement, the corresponding displacements can be compared directly. In addition, a mechanical regularization of the FE-SDIC measurements allows mechanically consistent fields to be evaluated, such as displacement and rotation fields that could be used as boundary conditions in the simulations. The experimental procedure, the measurement methodologies and the calculation/test dialogue are validated on isotropic metal plates in this paper.

1. State of the art and positioning

Composite structures are now well established in the field of civil and military aeronautical structures. Their mass percentages for the Boeing 787 and the Airbus A350 XWB are greater than 50% and that of the aerodynamic surface is close to 100%. In practice, the development and certification of these structures is still largely based on experimental validations in an approach known as the pyramid of tests (Fig. 1, Rouchon [1]). The base of the pyramid, at the coupon level, permits allowable values and their scatter to be obtained, which enable A and B values to be calculated. Tests are performed on coupon specimens under uniaxial stresses. The upper levels of the pyramid involve structural tests on more specific specimens that are more representative of the designs, but always under uniaxial loading. In addition, for composite structures, sizing and damage tolerance methods were developed as part of the certification of the first composite primary structure

certified on a civil aircraft, the ATR 72 wing box (Tropis et al. [2]) and must also be validated by the pyramid of tests. However, these methods, although they have the advantage of being robust, have the disadvantage of being extremely costly (tens of thousands of tests per aircraft) and generating very long design cycles. Also, a major challenge for future programs is to significantly reduce the number of tests and design loops and thus actually shift towards "Predictive Virtual Testing". It is with this objective that the "VERTEX" program was funded by the French National Research Agency [3]. VERTEX is the French acronym for "Experimental Modeling and Validation of CompositE stRucTures under complEX loading".

Nowadays, in terms of predictive virtual testing, a number of modeling strategies are relevant and are beginning to be predictive. Several approaches are based on continuum mechanics and damage mechanics: the "mesomodel" developed initially at LMT Cachan [4] and the ONERA model (ranked "best model" in WWFE 3 [5,6]), among others [7,8]. The authors of these articles (the present article and its second part) initially developed the Discrete Ply Model method to deal with out-of-plane issues such as low energy

* Corresponding author.
  E-mail address: bruno.castanie@insa-toulouse.fr (B. Castanié).

impact [9,10] and pull-through [11]. This type of method is also efficient for in-plane stresses [12,13]. It is mainly based on a mesh imposing *a priori* rupture paths, which makes it possible to take splitting and intra and inter-laminar interactions into account. To avoid the main drawback of this method, which is the difficulty of meshing structural singularities, strategies based on elements with phantom nodes [14–16] or regularized X-FEM seem promising [17]. Very recently, a method based on floating nodes has also
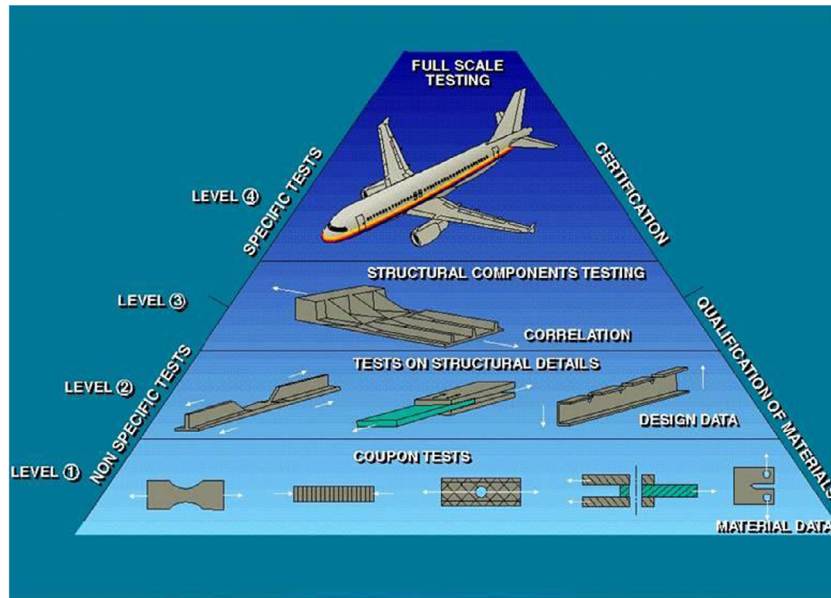

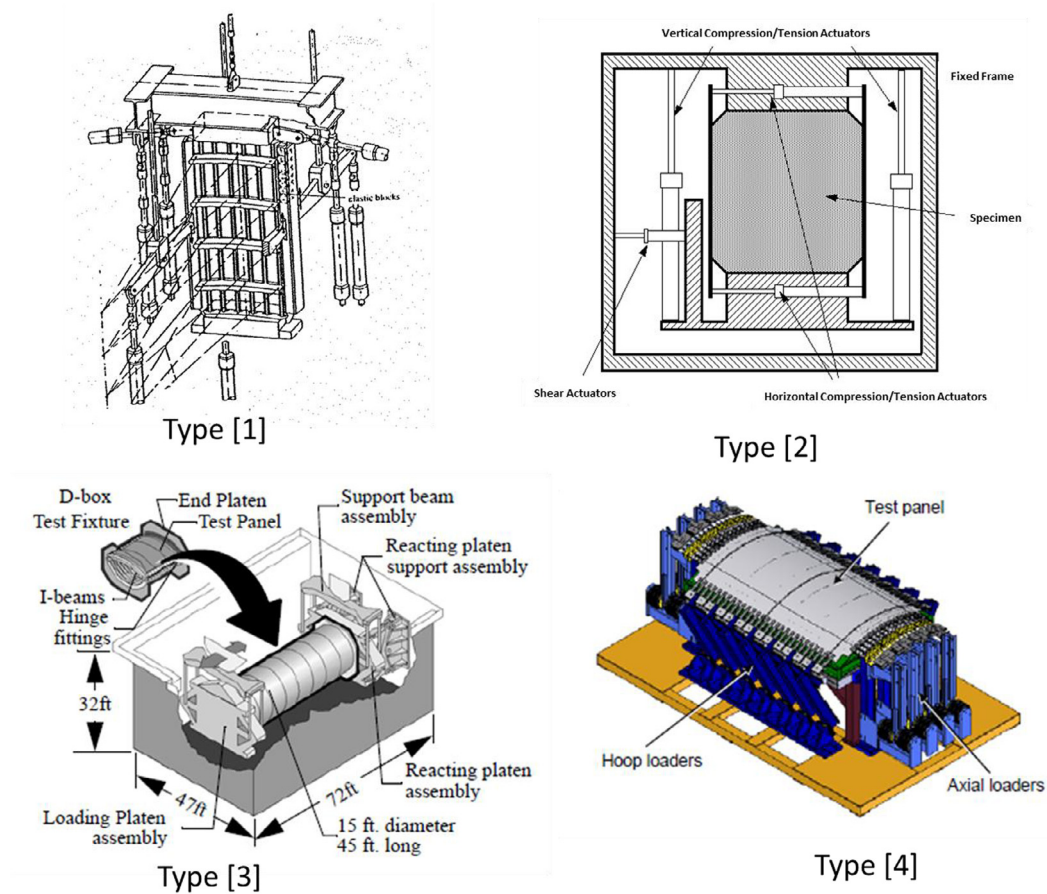
Fig. 1. Pyramid of tests.

Fig. 2. A few pictures of combined loading testing machines (extracted from [25,26,29,31]

been developed [18]. An alternative approach using peridynamics for modeling the damage of composite structures was used by Madenci and his co-authors [19,20]. These modeling strategies have reached a high level of maturity but have been applied only to restricted, academic problems, i.e. to coupon-type specimens subjected to uniaxial loadings. However, some recent studies have also focused on more structural issues. Bertolini et al. carried out 7-point bending tests to simulate stiffener detachment and uniaxial stress tests in compression and shear at the structure scale [21] in the context of certification tests. Recently, a specimen called the "single stringer specimen" was developed at NASA Langley. Tests with this specimen, more representative of real structures, allow the damage after impact to be studied in interaction with postbuckling and the issue of delamination migration at the bottom of the stiffener [22,23].

Multiaxial tests on coupons have been developed and identified by Olsson [24]. In this study, we are interested in the damage of composite structures at the scale of the structure and, in particular, under complex stresses. There are relatively few test rigs of this type in the world, and even fewer open publications. The main studies at this level are related to the problems of stiffener debonding or stability analysis of stiffened aeronautical or space structures. There are two main families of machines. The first directly reproduces the compression/shear loads by means of actuators. Wolf and Kossira [25] have presented a machine for testing fuselage skin panels (see Fig. 2, type 1). They do not mention the
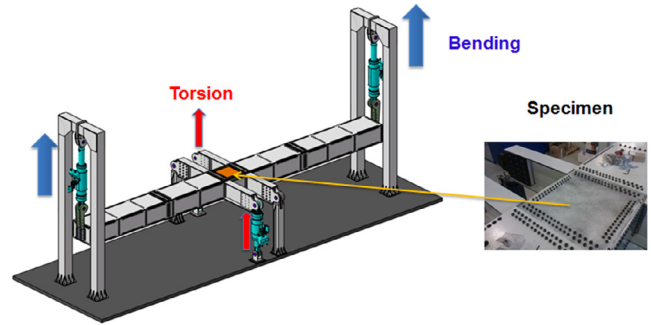

Fig. 4. Vertex test rig.

advantages and drawbacks of this method, but it is obviously technically complex and requires 10 actuators to operate. Another machine that can provide both biaxial tension/compression and shear was developed for structures used in the space industry [26] (see Fig. 2, type 2). The specimen has a surface area of about 1 m². The actuators are controlled by position sensors, thus avoiding any rotation of the free fixture or introduction of parasite loads. This machine uses just one of the sides to introduce the shear load, and it can be observed that the loading is closer to bending with shear than to pure shear.
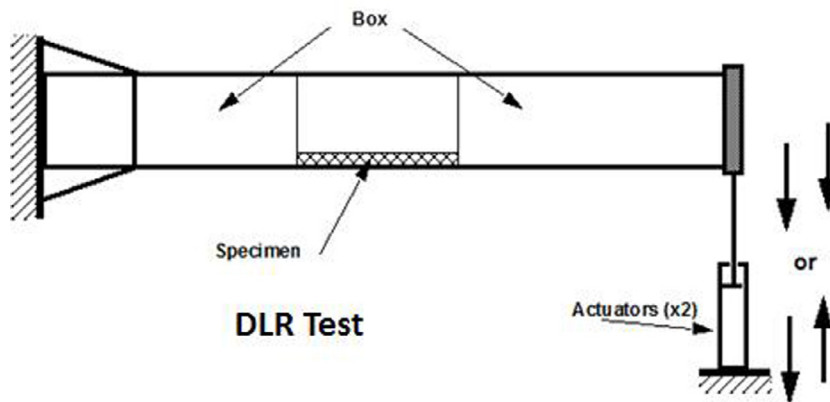
Fig. 3. Box based combined loading test rig.

Load Case	Loading	Laminate
1	Max Pure Compression 3000 N/mm	70/10/10/10
2	Max Pure Traction 3000 N/mm	70/10/10/10
3	Shear 1000 N/mm	10/40/40/10
4	Max Internal pressure 1.6 bar	40/10/10/40
5	Compression + Shear 1000 N/mm each	25/25/25/25
6	Traction + Shear 1000 N/mm each	25/25/25/25
7	Case 1 + Internal pressure	70/10/10/10
8	Case 2 + Internal pressure	70/10/10/10
9	Case 3 + Internal pressure	10/40/40/10
10	Case 5 + Internal pressure	25/25/25/25

Another type of machine is based on the use of a box to subject a specimen to combined loads. NASA Langley has the COLTS (COmbined Loading Testing System [27,28]) which allows aeronautical structures to be tested under multiple combined loads. Coupled to a D-Box, it can test large fuselage panels with internal pressure [29,30] (see Fig. 2, type 3). The dimensions of this equipment are very large (72 ft or about 22 m). A test facility initially designed to study internal pressure fuselage fatigue was developed by the FAA (Faster Test Facility) and has recently been upgraded to allow combined loads with shear [31] (see Fig. 2, Type 4). Dimensions here seem to be of the order of a square meter. The concept of using a box to create an internal pressure and additional actuators to superimpose other loads has also been taken up by Best et al. [32]. In the machines they present, the panels are large and curved, which makes the tests quite complex and costly so they would tend to be reserved for validations near the top of the pyramid of tests.

An alternative solution is to use simple rectangular boxes. This idea is far from new: as early as 1948, Peters [33] subjected a square sectioned box to torsion and bending and was thus able
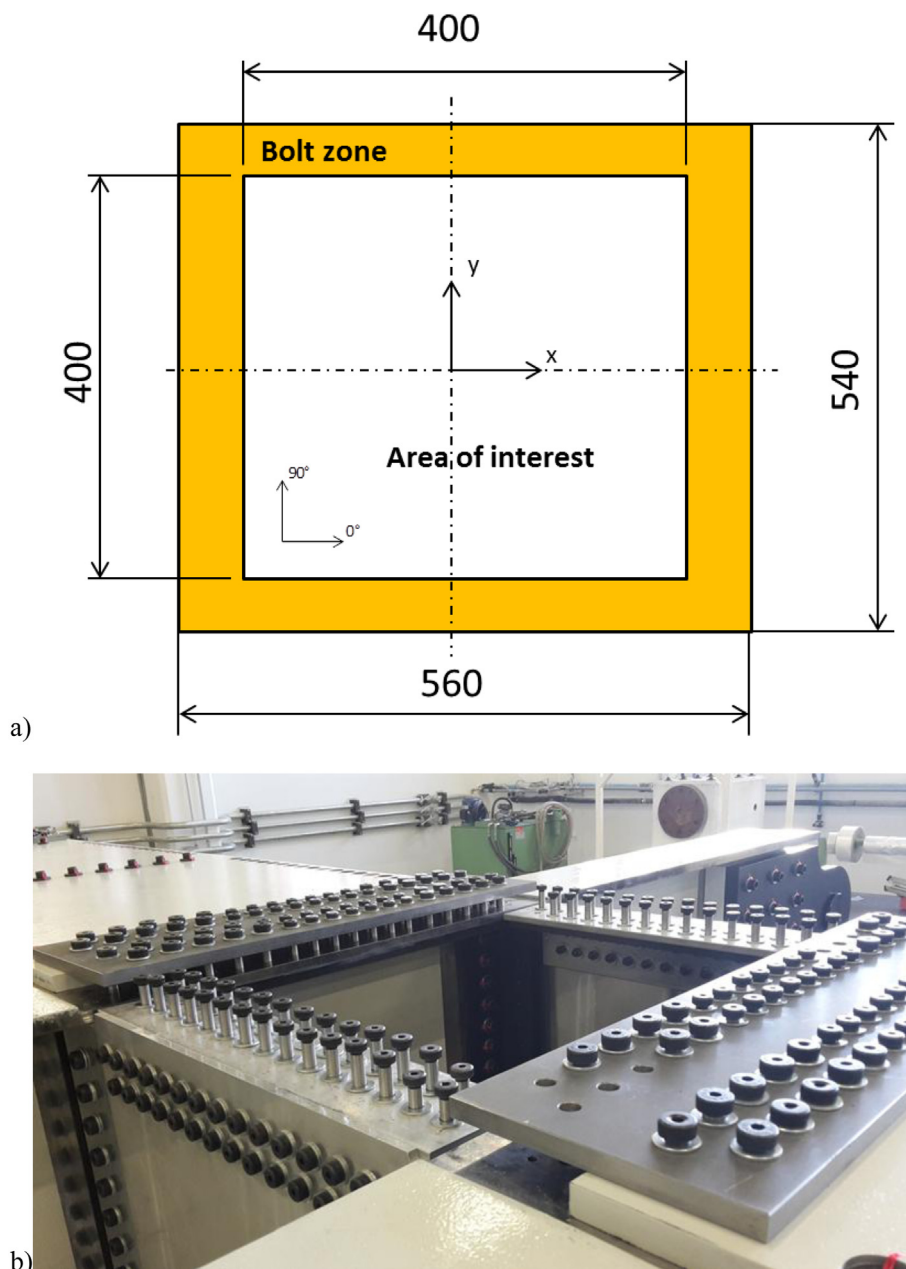

Fig. 5. Bolted area of the specimen (a) and final design (b).

to identify an experimental curve of the compression/shear buckling of the specimens making up the faces of the central part of the box. More recently, Klein [34] used a box structure clamped to a support at one end and loaded in bending/torsion at the other end by means of two actuators (see Fig. 3, DLR Test). When the two actuators are activated symmetrically, the box is loaded in bending. In this case, the lower box face, where the sample is mounted, is subjected to tensile or compressive stresses (and also to transverse shear). When the two actuators are activated antisymmetrically, the box is subjected to torsion and the specimen, which acts as a membrane, takes shear. Because the actuators are controlled, the two types of loading can be combined. The laminated or sandwich composite specimen is 1 m long and is bolted to the box by 180 bolts and a resin interface. This ensures that the real boundary condition is very close to the "all-clamped" theoretical model, since the box itself is very rigid. Klein claims to have obtained good results for determining critical buckling loads for 6–8 mm thick sandwich plates. He points out that it is impossible to determine the stress resultants entering the sample because of the numerous structural redundancies. However, the flow is measured in situ by equipping the specimen with 150 strain gauges set out in a grid pattern.

Castanié et al. [35,36] developed a complex loading test method for asymmetric sandwich structures (Fig. 3, Castanié's test). This is detailed in paragraph 2.1. Static tests were carried out under compression, shear and combined compression/shear stress on both pristine and impacted specimens. These tests have demonstrated that asymmetrical sandwich structures have exceptional compressive and impact behavior. In particular, the boundary conditions of these structural tests are very different from those of conventional Compression After Impact (CAI) tests [37] and are very conservative because, once the damage has initiated, it quickly propagates to the free edges. Tests at this level have the characteristic of being less conservative and more representative than the normalized uniaxial tests. However, in the conclusion to [36], it was emphasized that the area of interest of the test machine was too small and that the Saint-Venant's effects were preponderant. In this test, too, it is very difficult to control the in-plane loadings actually entering the test piece, a problem already identified by Klein [34].

This overview of the state of the art clearly shows that a new field of research is opening up to investigate composite structures at the scale of technological specimens and under complex loads. The following section describes the different stages of development of a new test device intended to meet this new challenge. As pointed out, if tests useful for the validation of damage models or for the analysis of failure scenarios are to be carried out, it is essential to be able to control and measure the actual in-plane forces in the specimen and to monitor damage during the test. So a measurement strategy called Finite Element-Stereo Digital Image Correlation (FE-SDIC) will be proposed in the 3rd section, where the validation tests on isotropic specimens and a reception test at 50% of the maximum load will also be analyzed. Finally, conclusions will be drawn from this first part of the study.
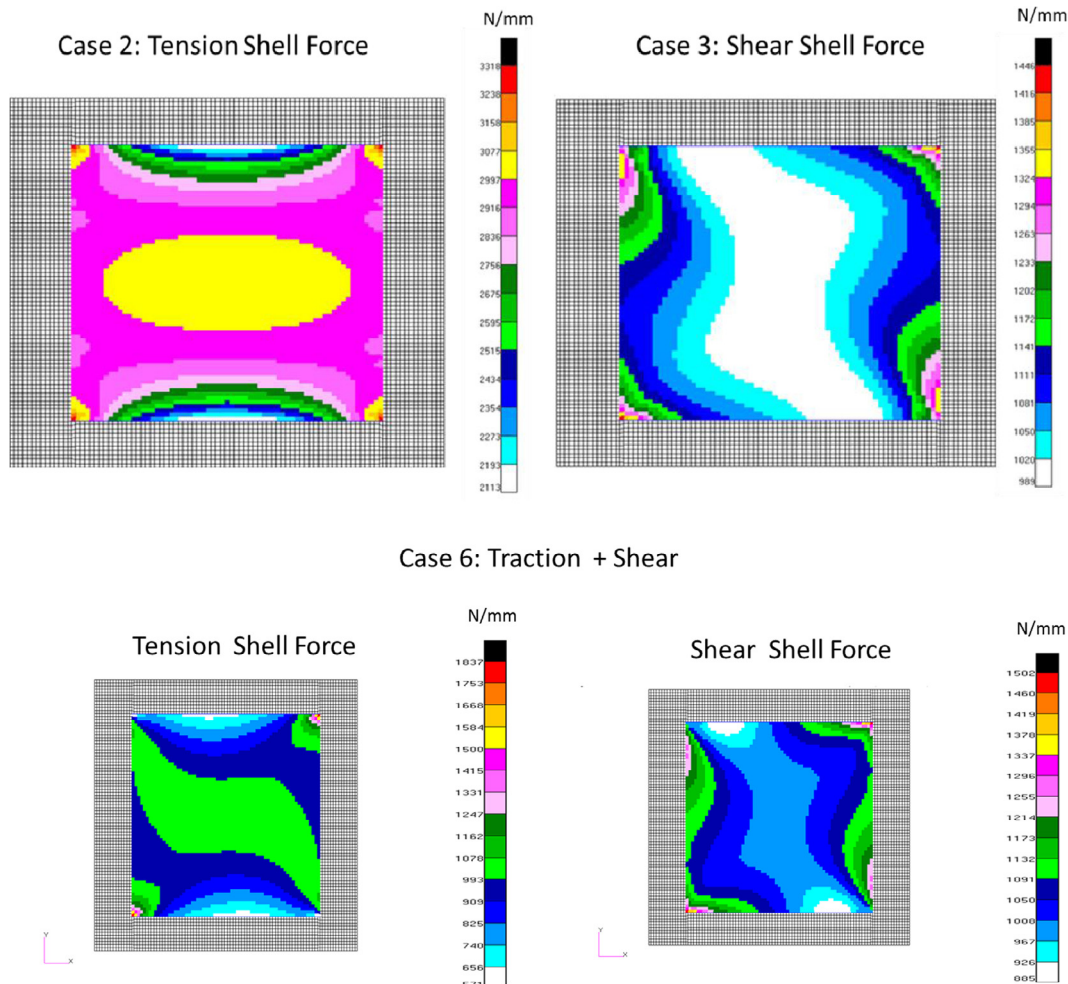

Fig. 6. Traction and Shear Shell Forces in the specimen (Cases 2, 3 and 6, see Table 1).

2. Development of the VERTEX test rig

2.1. Choice and description of the architecture

The first parameter to be determined is the size of the specimen. The previous section concluded on the scale of the technological specimens. A test piece must be capable of representing the physical phenomena and the composite technologies involved but must not be specific to a particular area of an aircraft. The choice of size is driven by the following compromise: the specimen must be large enough to represent the structural problems and to limit the Saint-Venant's effects while being small enough to keep costs within reasonable limits. In [36], the size of the area of interest was 200×200 mm^2, which was too small. In the other machines described, the size of the test pieces was of the order of one square meter, which is necessary to represent fuselage sections but is too large and too expensive for a technological test piece. Finally, dimensions were chosen in the area of 400×400 mm^2 which seems the best compromise *a priori*. The second parameters to be determined are the loads applicable to the test specimens. An exchange with industrial partners in commercial aviation, space, defense, and helicopters made it possible to select fluxes of

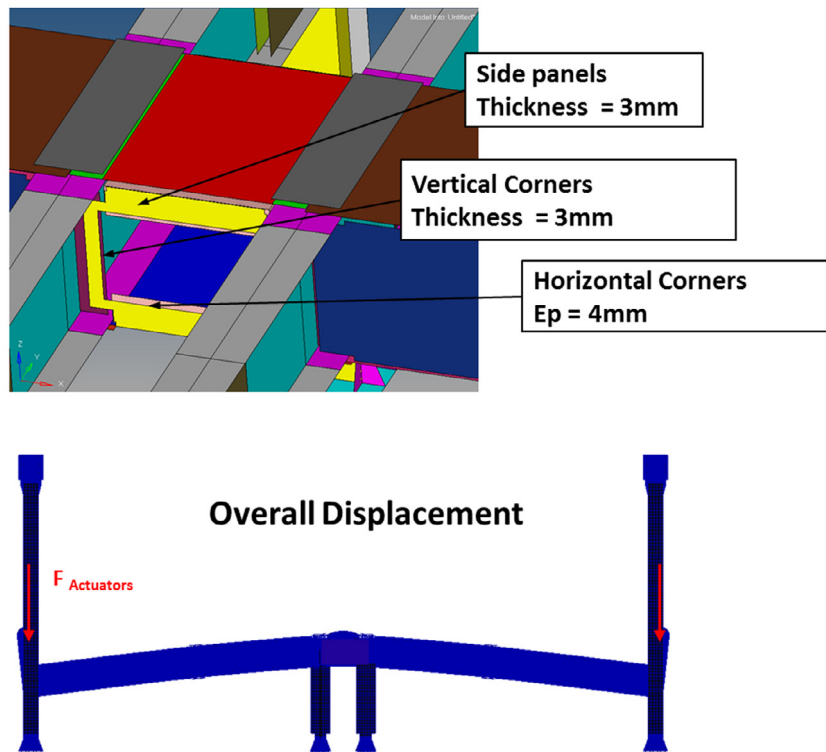### Case « Soft » n°1: tension on a specimen with a thickness of 2,5 mm

Side panels
Thickness = 3mm

Vertical Corners
Thickness = 3mm

Horizontal Corners
Ep = 4mm

Overall Displacement

F Actuators

Fig. 7. "Soft central box case". Design of the corners of the side and overview of the displacements of the FE model.

Fig. 8. Monitoring screen for actuators.

3000 N/mm in tension/compression and 1000 N/mm in shear, and an internal pressure of 1.6 bars.

The literature review has shown that two types of architecture are possible: loading can be either direct or applied with the help of a box. If a direct load of 3000 N/mm is used on a 400 mm test piece, the load to be exerted is 1200 kN. Actuators of this type exist but are extremely expensive and could exhibit driving problems for small displacements. In addition, decoupling systems would be complex to design, manufacture and implement. Clearly, a box type solution is preferable and the experience gained in [36] will be paramount. The principle of the device is described in Fig. 4. The machine consists of a longitudinal box and two cross beams. The test piece is bolted to the upper face of the box between the two I-beams. Four actuators and two support legs are used. The two actuators at the end of the box place the assembly in 4-point bending and the specimen in tension or compression. The two actuators at the end of the I-beams put the central part of the box in torsion and the test piece in shear. A bladder-based system inserted into the central box between the I-beams allows the test piece to be subjected to internal pressure. The device is bolted onto a very rigid steel support 3 m wide and 9 m long.

2.2. Sizing policies and design loops

The design process is complex and involves design loops. The first phase of pre-sizing using beam theory allowed the dimensions

Fig. 9. Overview of the VERTEX test rig.

Fig. 10. Detail of a specimen bolted onto the upper part of the central box of the VERTEX test rig.

of the box and the loads of the jack to be approximately defined from the constraints of overall dimensions and the required loads. Given the manufacturing delay, the design of the actuators was fixed early, with a 280 kN load and a stroke of 240 mm for the bending actuators and 250 kN load and 110 mm stroke for the torsion actuators. For the detailed design, several Finite Element (FE) models of increasing complexity were created and analyzed. Ten loading cases have been selected and are listed in Table 1. The virtual test specimens are based on 5 mm thick UD carbon/epoxy lay-ups and the stacking sequences are adapted to the type of load. The first step consisted in defining the attachments of the specimen in the envelope of the maximum loads. After several iterations, a
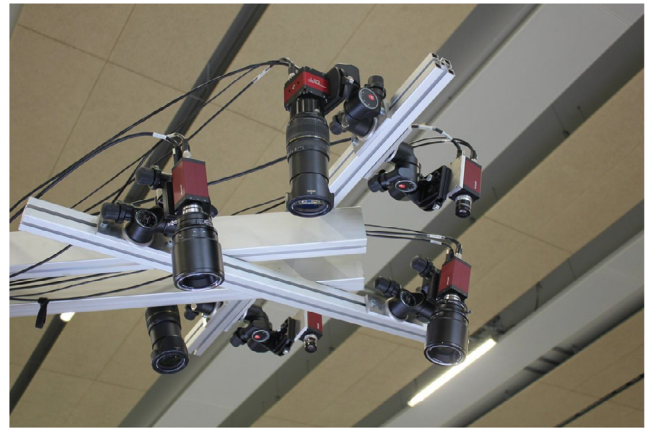

Fig. 11. View of the six cameras used to monitor the tests. They are mounted on a jib above the specimen.
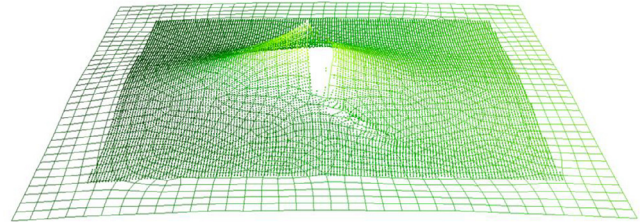

Fig. 12. Comparison of the S-DIC measurement using a classic subset approach (dots) and the proposed Finite Element formulation (mesh) on a composite plate subjected to a Vertex tension test.
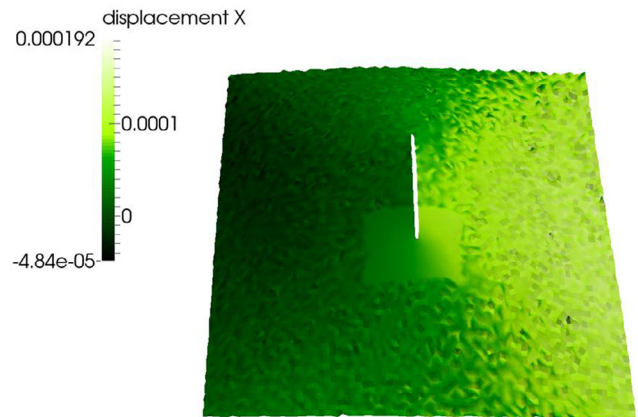

Fig. 13. Multiscale FE-SDIC measurement using 4 cameras: 2 in far-field view and 2 in nearfield view close to one crack tip.
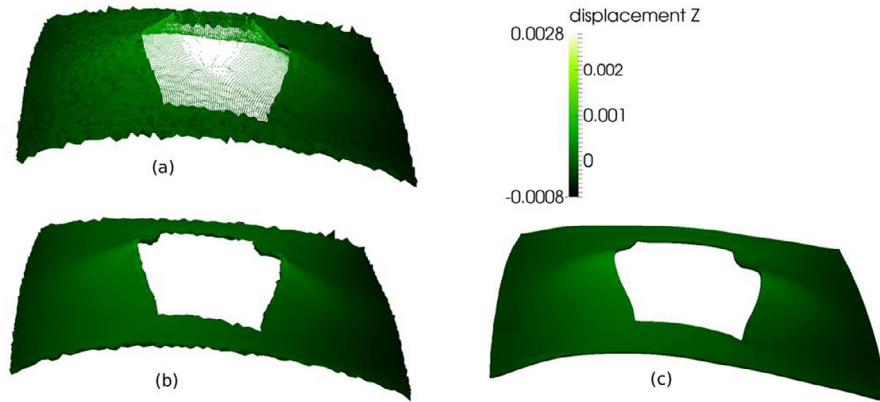
Fig. 14. Displacement measurement in the reliable zone of a composite specimen subjected to a Vertex tension test using classic DIC (a) (dots), FE-SDIC (a) (plain), mechanically regularized FE-SDIC (b) and integrated FE-SDIC (c).

bolting zone of external dimensions 560×540 mm^2 has been defined (Fig. 5.a) and 128 fasteners, 8 and 10 mm in diameter, are required (Fig. 5.b). The local thickness of the test piece in this zone will depend on the stresses. For the highest loads, double shearing of the fasteners is necessary as shown in Fig. 5.b.

With the exception of the central box, the device has been sized with a static safety factor of 2 with respect to the elastic limit or the buckling loads. The center box is treated differently. The experience of [35] shows that it is necessary to allow the assembly to plasticize locally in order to follow the strains of the carbon specimens. Moreover, the stiffness of the central box must be adapted to the type of load. The lateral flanks are made of aluminum alloy for the bending stress of the box so as to favor the compressive or tensile flows in the test piece. In shear, the flux inside the central box is constant and it is necessary to maximize the torsional stiffness, so the lateral flanks are made of steel. The junction brackets are also suited to this purpose.

The first objective was to validate the concept to reach the maximum stress resultants in the specimen. A complete FE model, including fasteners, was developed and linear and nonlinear geometric computations were performed. The membrane stress resultant fields for loading cases 2 and 3, in tension and in shear, respectively, are given in Fig. 6. The combined case of tension + shear is also given in Fig. 6. It can be noted that the maximum values are achieved within the domain of use of the jacks and, moreover, the strain fields are substantially homogeneous in the center of the test piece. In this type of test, however, it is unrealistic to expect a perfectly uniform field over the whole specimen because the boundary conditions are more complex than in uniaxial tests conducted on elementary specimens. This unavoidable heterogeneity should not be seen as a disadvantage of this type of test, but rather as new, intrinsic data of such structural tests

The problem of these new structural tests is also that the variety of behaviors to be tested is large and that it was necessary to verify that the test assembly also made it possible to test thinner parts until failure. In particular, experience has shown that it is necessary to verify the ability of the assembly to generate strains greater than 10,000 μstrains in the range of use of the actuators (stress and stroke). Several "soft center box" cases have been virtually tested. The first, described in Fig. 7, shows how the central box is adapted by reducing the thickness of the lateral flanks. For a test specimen [10/4/4/2] in tension with a thickness of 2.5 mm, at 260 kN, there is a strain at the center of 18,100 μstrains and an actuator stroke of 110 mm. In compression, with the same type of specimen but in a sandwich configuration (thickness of skins 1 mm, thickness of core 32 mm), the maximum compression stress resultant in the test piece (3030 N/mm) is reached for a stroke of 98 mm less than
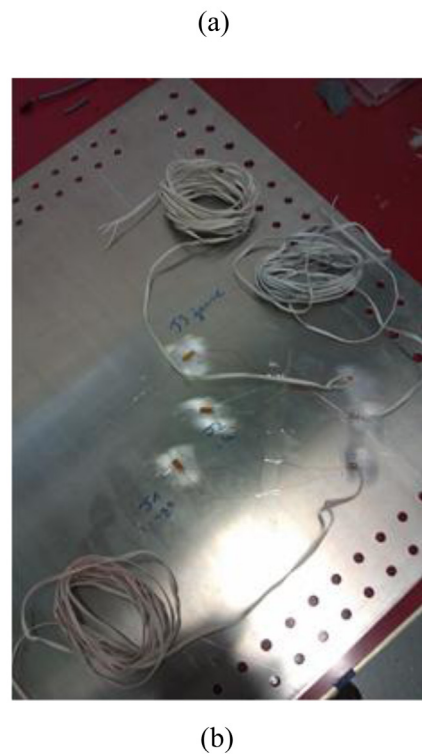
(a)

(b)

Fig. 15. (a) View of the hidden side of the aluminum test piece with three strain gauges oriented at 0°, 45° and 90°. (b) View of the specimen bolted on the VERTEX device.

the maximum stroke of the actuators (260 mm), and the maximum strain at the center of the specimen reaches $-17,000$ μstrains. Approximately 6 months of studies were necessary to finalize and validate the design and the sizing of this structure.

2.3. General characteristics

The test device has its own hydraulic unit. The 4 actuators are driven in classical force or displacement control but specific features have been included. In particular, starting from displacement control of a bending actuator, it is possible to impose equal loading forces on the two bending actuators:

$$F_{Actuator\ Bending\ 1} = F_{Actuator\ Bending\ 2}$$

and similarly for torsion actuators:

$$F_{Actuator\ Torsion\ 1} = F_{Actuator\ Torsion\ 2}$$

Moreover, it is possible to ensure the theoretical static equilibrium of the assembly by driving actuator 1 in displacement and then:

$$F_{Actuator\ Bending\ 1} = F_{Actuator\ Bending\ 2} = 2 \times F_{Actuator\ Torsion\ 1}$$
$$= 2 \times F_{Actuator\ Torsion\ 2}$$

Specific software has been developed for control. Its graphic interface is shown in Fig. 8. Twenty-four measuring channels are incorporated and supplementary measurement channels are also provided that can be used for controlling the equipment. A long-term objective is to be able to drive a composite failure test using measurements of kinematic fields obtained by FE-SDIC. Specific failure paths could thus be generated with the experimental procedures of this test.

A general view of the assembly is given in Fig. 9. It is 8.5 m long, 2.9 m wide and 3 m high. Approximately 2000 bolts are used. The cost of this assembly (studies, manufacture and assembly) is about 500 k€. A transparent safety box is added before launching the test to protect against spattering of carbon particles following high energy breaks. A detailed view of a test specimen attached to the assembly is given in Fig. 10. A support is installed above the central box with 6 cameras to monitor the tests by FE-SDIC (Fig. 9 and Fig. 11). The strategies used to analyze the pictures taken by these six cameras are presented in the following section.

3. DIC instrumentation and experiment/simulation coupling

As mentioned above, the monitoring of structural tests is generally achieved using many strain gauges, see [34–36]. Although this type of instrumentation can provide extremely accurate measurements, it has various drawbacks. First, the technique only gives access to sparse information. Moreover, it is not always easy to choose the size of the gauges and their position and, consequently, to assess local strain gradients. Gauges can sometimes be rather laborious to implement and do not always ensure that the experiment is followed until rupture.

Among these limitations, the most restrictive is certainly the inability to obtain an experimental determination of the load fluxes or more generally the actual boundary conditions (BC) prescribed for the specimen [34,36]. That is even more true in the context of the buckling of composite shells since their behavior is highly sensitive to geometrical and loading imperfections.

3.1. Initial shape and displacement measurements

In this study, in order to cope with both geometric and loading imperfections, the idea is to perform displacement-driven simulations using the experimentally measured displacements and geometry. For this purpose, the Vertex experiments are instrumented
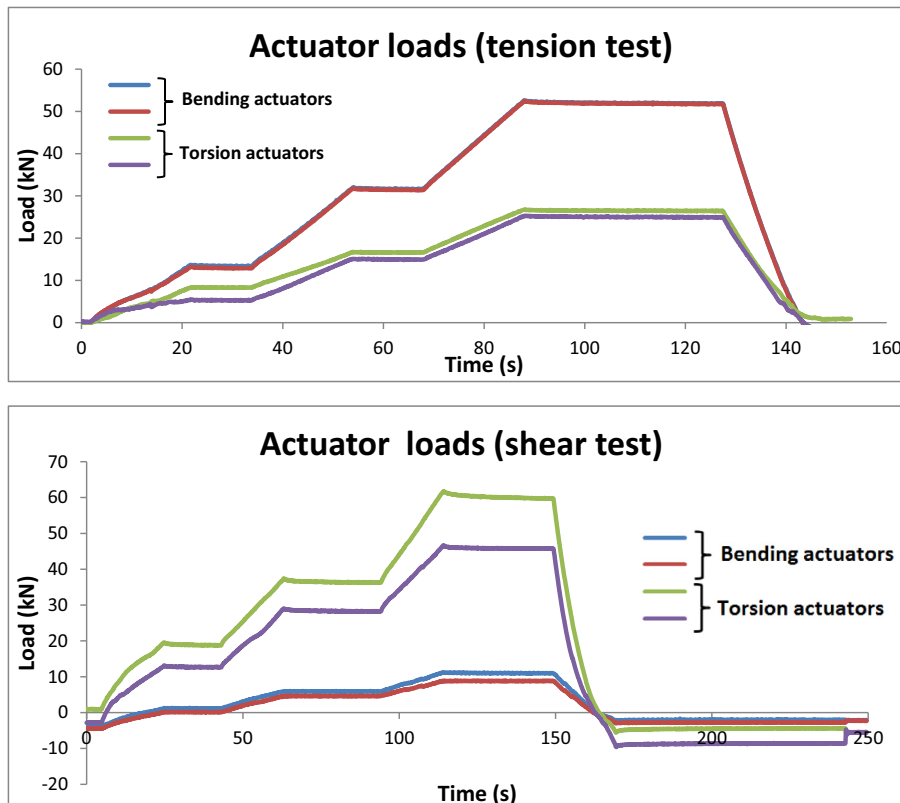

Fig. 16. Load vs Time for tension and shear tests driven by displacement.

using Stereo Digital Image Correlation (SDIC [38]). This technique classically gives access to the shape and 3D displacements of the top surface of the specimen.

In consequence, standard SDIC software cannot solve the above problems completely. First, as stated above, usual SDIC is not able to measure the displacement in the bulk of the specimen, and, in this particular case, out-of-plane rotations cannot be measured directly. The second reason is that comparing measured and simulated kinematic fields is not an easy task as the computed and measured fields are (a) not expressed in the same coordinate system, (b) generally not based on the same kinematic descriptors and (c) not defined on the same domain. Quantifying the distance between simulated and measured kinematic fields requires a set of projections and interpolations and this is not acceptable when the sources of errors need to be precisely quantified.

To circumvent these difficulties, a global FE-SDIC algorithm was developed during the Vertex project [39]. This method uses an FE interpolation for the SDIC problem. With this tool, it is possible to use the same mesh as the one used to avoid the aforementioned projections. More precisely, the unknown displacement field, U, is still the solution of a quadratic minimization problem associated with the gray level conservation equation between reference image f_c and deformed state image g_c for all cameras c. However, unlike the situation with classic SDIC algorithms, here, the problem is written in the coordinate system of the mesh of the specimen [40,41]:

$$U^* = \arg\min_U \phi_{dic}^2(U) \quad \text{with}$$

$$\phi_{dic}^2(U) = \sum_c \int_\Omega [f_c(\mathbf{P}_c(\mathbf{X})) - g_c(\mathbf{P}_c(\mathbf{X} + \mathbf{U}))]^2 \, d\mathbf{X}$$

where $\boldsymbol{P}_c$ is a possibly non-linear camera model that maps a 3D point $\boldsymbol{X}$ to the associated 2D position in the image plane. In addition, a Galerkin formulation of the SDIC problem is written. It allows FE to be used for the approximation of the measured displacement, as is done in simulation. For instance, Fig. 12 shows the good match between the displacements measured using this FE method and a classic SDIC.

In such a projection-free framework, validation simply requires the direct comparison of measured and simulated degrees of freedom node by node on the FE mesh. Such formalism can also be used for shape measurement and calibration. (See [39] for more details.)

In practice, the idea would then be to provide the user with displacement fields that are well suited to the validation of his model, exploiting his own mesh. However, a mesh optimized for simulation is not necessarily suitable for measurement. To bring additional information where the size of the elements would become too small in comparison with the correlation length of the texture, the idea is to exploit images having locally better resolution. The feasibility of multi-scale FE-DIC measurements in a context of identification has been demonstrated in 2D [14].

The extension of this approach to the case of the structural tests presented in this paper was made possible thanks to the newly developed FE-SDIC. This formulation can naturally handle more than two cameras because it does not make use of the master–slave camera formulation of standard SDIC methods. Here, a cluster of six cameras mounted on a rigid jib was installed above the specimen (see Fig. 9 and Fig. 11).

Two 5 Mp cameras record images from the whole specimen in order to estimate boundary conditions (necessary for a realistic simulation), while two other 5 Mp cameras zoom in on the region where the model will be validated. Two additional very high resolution cameras were also used to record the entire central region of the specimen, but they are not actually exploited in this article.

Fig. 13 shows a displacement field obtained from the first four cameras. There is a clear noise reduction in the nearfield zone as compared to the rest of the region of interest [39].

3.2. Identification of boundary conditions

As stated previously, since the numerical simulations are sensitive to BCs (especially in the presence of buckling), displacement-driven simulations were chosen. To be able to correctly impose the moments at the edges of the region under study, Sztefek and Olsson [44] have proposed, for example, that out-of-plane displacement should be imposed on the nodes located in a band around the studied region. They thus avoid a noise sensitive derivation of the measured displacement field.

With the Stereo FE-DIC [39], it is possible to go further. The tool makes it possible to measure displacement fields regularized by a mechanical model [41,42]. In a zone assumed to remain elastic (which is relevant far from the central notch), later called the "test body", the displacement field that minimizes a weighted sum (λ) of the gray level functional ϕ_{dic} and a mechanical function ϕ_{mech}

Fig. 17. Failure pattern of a thick notched composite specimen under tension.

(based on the stiffness operator associated with the same mesh and elastic linear elastic behavior) is sought [39]:

$$\mathbf{U}^* = \left\{ \underset{\mathbf{U}}{\arg\min} \right\}, \{ \phi_{dic}^2(\mathbf{U}) + \phi_{mech}^2(\mathbf{U}) \}$$

With this method, proposed recently in [39], and called "regularized", the displacement field $\mathbf{U}$ is not limited only to the upper surface. By assuming an elastic medium and taking the surface observations into account, it is possible to measure the displacement in the volume of the test specimen. With an FE plate model, it is thus possible to measure rotations in addition to displacements.

In this paper, a new "integrated" digital correlation technique is proposed. This consists in recording images (gray level conserva-tion) using a displacement field $\mathbf{U}$ obtained from a displacement-driven simulation using $\mathbf{V}_{BC}$ as boundary conditions. The field of boundary conditions $\mathbf{V}_{BC}$ is then the only unknown of a DIC-like optimization problem.

$$\mathbf{V}_{BC}^* = \underset{\mathbf{V}_{BC}}{\arg\min} \, \phi_{dic}^2(\mathbf{U}(\mathbf{V}_{BC})) \quad \text{with} \quad \mathbf{U}(\mathbf{V}_{BC}) : \mathbf{V}_{BC} \underset{FEA}{\longrightarrow} \mathbf{U}$$

This method is termed "integrated" with reference to the integrated 2D FE-DIC method developed in [43], in which the optimization variable groups together the constitutive parameters that are sought. Assuming that this technique is applied in the "test body", it is possible to access a kinematic field in the bulk which respects the balance and minimizes the gray level conservation. Fig. 14 compares the displacement fields obtained with the
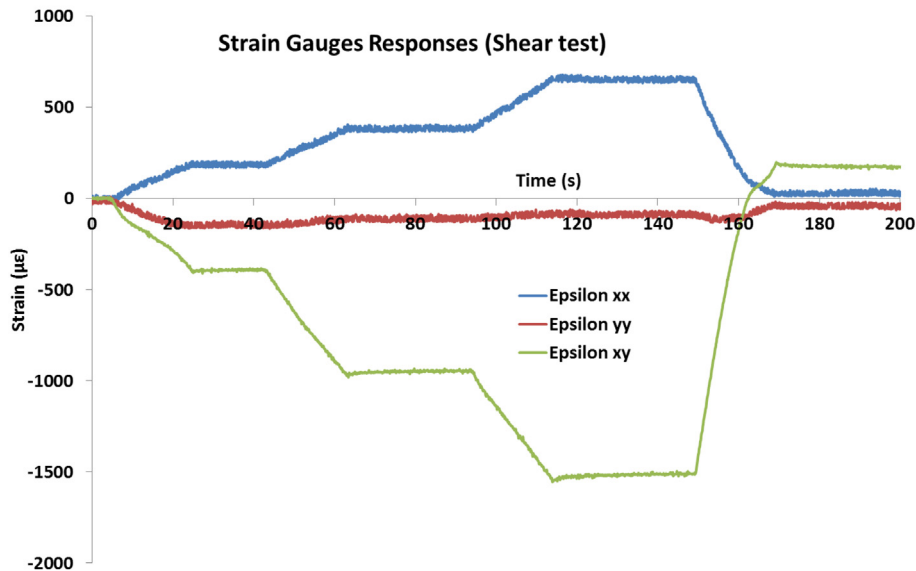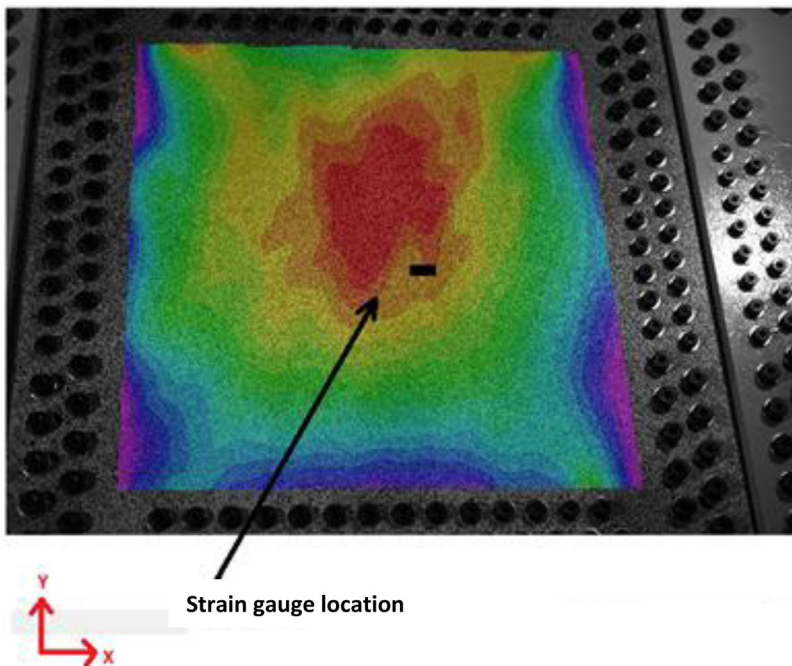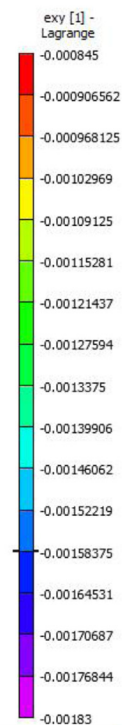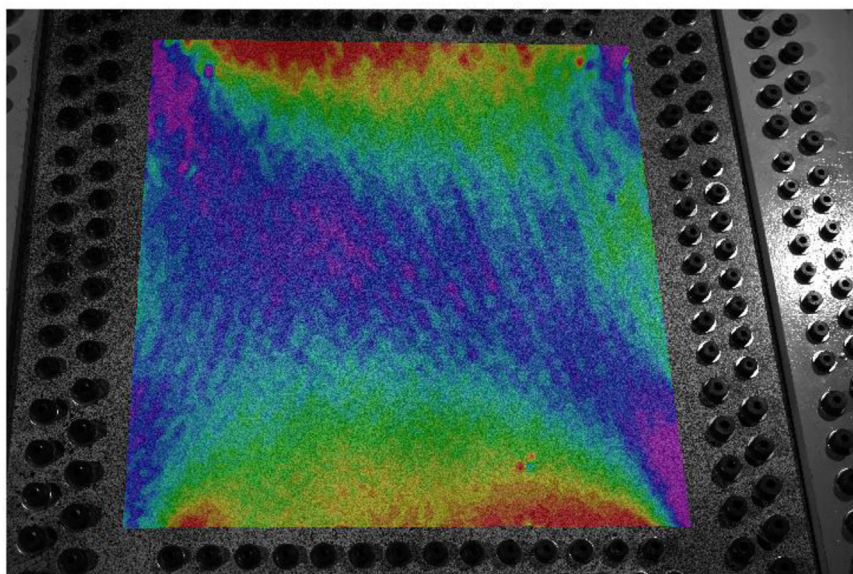
(a)
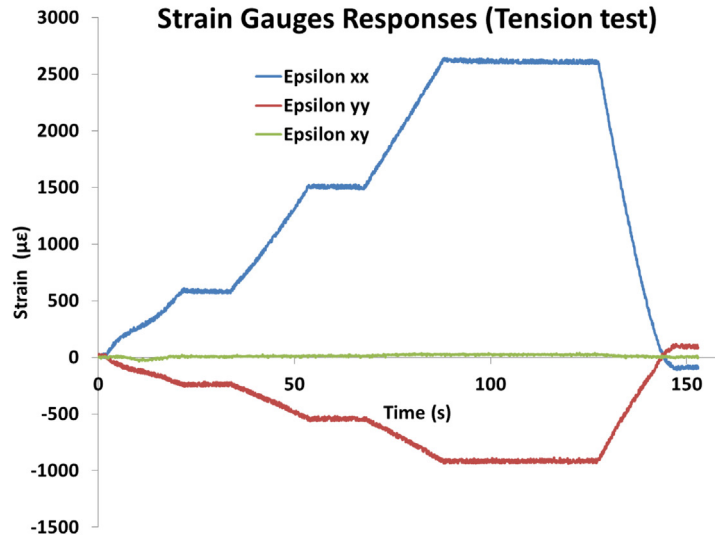
(b)

Fig. 18. Strain gauges responses for traction and shear tests on aluminum.

ε_xx (tension)

Strain gauge location

ε_xy (Shear)

(50.5475, 50.6614, 6.85568): -0.00158322

Fig. 19. VIC-3D© map responses for tensile and shear tests on aluminum plates at maximum loadings.
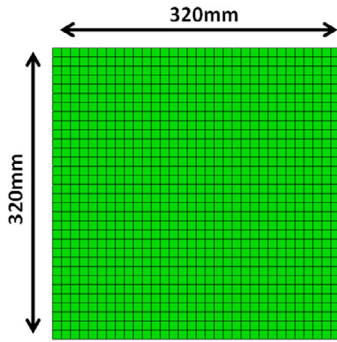
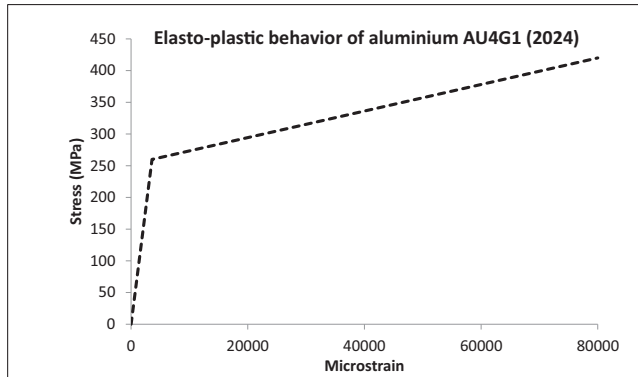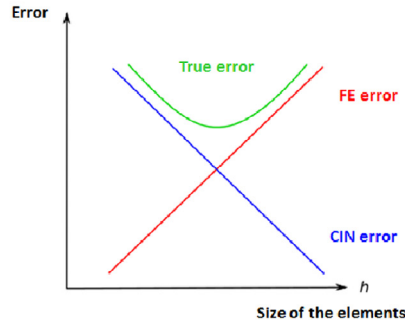**Fig. 20.** Mesh of the aluminum plates and choice of the size of the elements.

Fig. 21. Elasto-plastic behavior of aluminum 2024.

conventional SDIC and FE (a), the regularized (b) and the integrated (c) methods.

It may be noted that the FE mesh used for the calculation seems too fine for the measurement since, in the absence of mechanical knowledge, the FE-SDIC produces a noisy field of displacements. When the measurement is regularized, the displacement field is more regular, except on edge nodes, which cannot be regularized mechanically [42]. Eventually, the integrated method provides a very regular displacement, since it comes from an FE calculation. Because the number of degrees of freedom is reduced, the problem of identifying boundary conditions is very robust.

4. Experimental validation and discussion

The objectives of the first tests were multiple:

(1) To validate the general functioning: assembly of the test piece, execution of the tests and correct loading of the specimen.
(2) To validate the methodology of specimen measurement by FE-SDIC, and the quality of the tests performed.
(3) To validate the dialogue between test and computation, and the method of data exchange between FE-SDIC and Abaqus numerical models.

To meet these objectives, it was decided to start by testing 2024 aluminum plates having a thickness of 5 mm. The plates were equipped with three strain gauges on the invisible face and a speckle on the upper face (see Fig. 15.a). For these tests, a commercial analysis software was used (VIC-3D© software) as well as the research code. Tests were carried out under tensile, compressive, shear and combined tensile/shear stresses. The internal pressure function was not tested. A high-load test was also carried out on an UD carbon-laminated test specimen, strongly oriented at 0° with a thickness of 5 mm, to validate the transfer of stress in the notched specimens and the behavior of the assembly under high loads. These various points are discussed in the following sub-sections.

4.1. General functioning

The mounting of the specimen requires a large number of bolts (128 in total, visible in Fig. 5). This number is required for the transmission of high stress resultants and generates a very hyperstatic structure. For the aluminum plates, the holes were drilled to +0.5 mm and the assembly could be carried out. Finally for the last carbon plate, it was not possible to accept such large clearance and the additional clearance was only + 0.1 mm. The test setup was
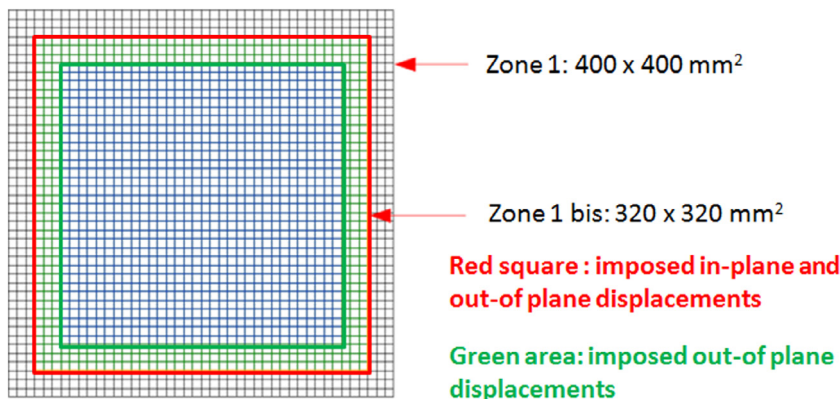

Fig. 22. Method of exchange of boundary conditions between FE-DIC and numerical model.
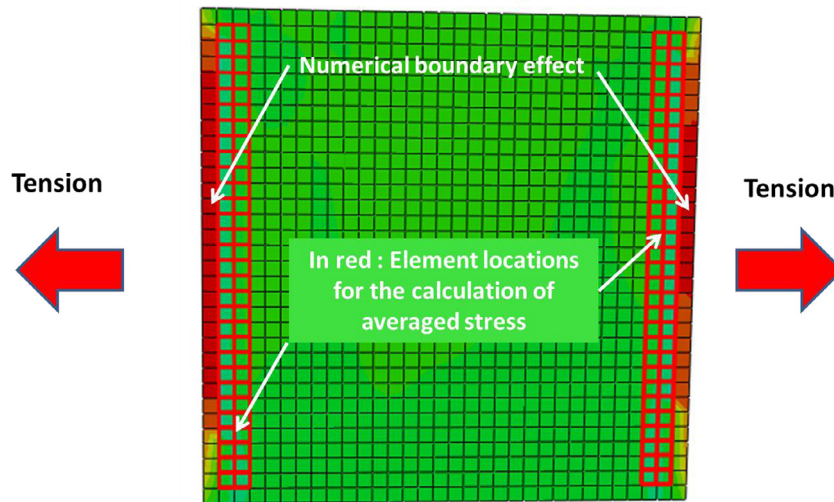
Fig. 23. Method for calculation of averaged stresses entering the plate.
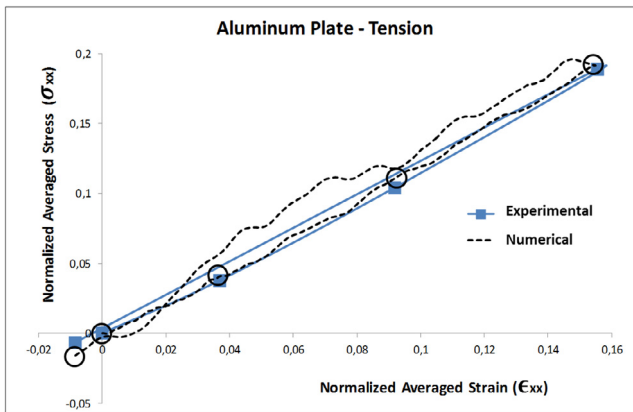

Fig. 24. Normalized averaged stresses vs normalized averaged strains for traction on aluminum plate.

assembled by bolting the plate on one of the 4 sides, then tightening the whole by successive adjustments. The strains obtained after tightening remained very moderate: maximum 300 μstrains, i.e. a few percent of the final failure strain in the case of composite plates.

Not all the PID corrector gain values had been adjusted when the VERTEX machine was delivered. One test led to the divergence of an actuator but, eventually, the adjustments ensuring correct stability were achieved. However, experience showed that, in the case of a bending stress, a fixed static equilibrium of the type:

$$F_{\text{Actuator Bending 1}} = F_{\text{Actuator Bending 2}} = 2 \times F_{\text{Actuator Torsion 1}}$$
$$= 2 \times F_{\text{Actuator Torsion 2}},$$

obtained with an actuator Bending 1 driven in displacement, was unstable around the reference position. This was due to a rigid body displacement of the assembly probably resulting from a free movement linked to the ball joints that fixed the actuators in torsion.
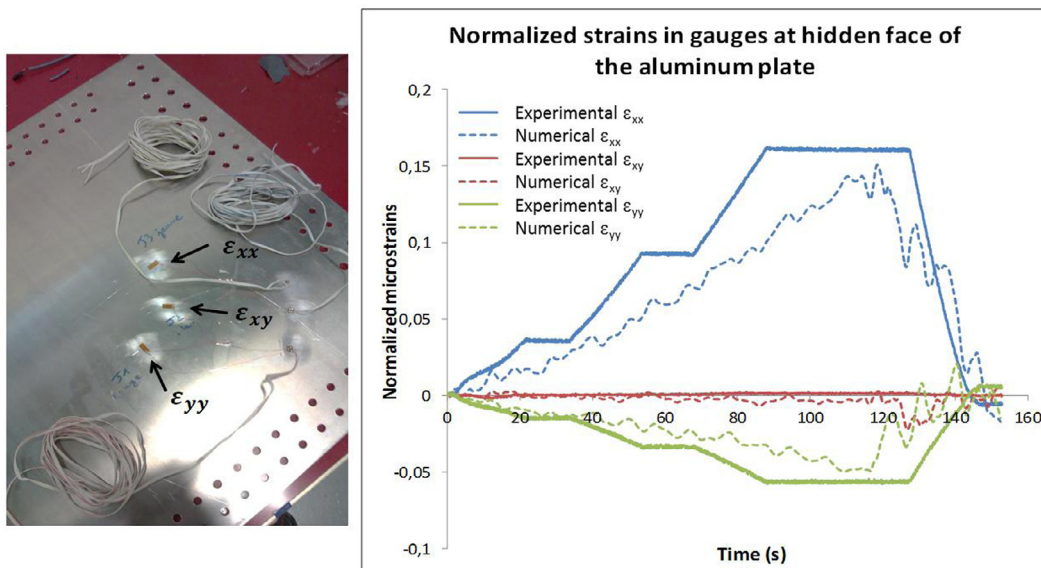

Fig. 25. Comparison of strains at the gauge locations for tension.

Since composite structure failures involve very high energies, the more prudent choice of driving the 4 actuators in displacement was made. However, this degrades the quality of the tests and will be discussed later. Curves of the forces exerted by the jacks as a function of time are given in Fig. 16 for a tensile test and a shear test on an aluminum plate. For the tensile test, a progressive displacement of the bending actuators and a zero displacement of the torsion actuators are imposed. For the shear test, a progressive displacement of the torsion actuators and a zero displacement of the bending actuators are imposed. For the tensile test, it can be seen that the theoretical result corresponding to the 4-point bending is reproduced experimentally:

$$F_{\text{Actuator Bending 1}} = F_{\text{Actuator Bending2}} = 2 \times F_{\text{Actuator Torsion 1}}$$
$$= 2 \times F_{\text{Actuator Torsion 2}}$$

It is also noteworthy that, for torsion, the imposition of a zero displacement on the bending actuators generates forces at about 10% of the torsional forces for a theoretical configuration equal to zero (after taring). This phenomenon is due to the out-of-plane displacement of the loading box which is countered by the zero-moving control of the bending actuators, which generates parasitic forces. This case had already been encountered in [35,36] and had been set manually. If it were possible to pilot these jacks in force, this phenomenon would be cancelled out, otherwise it would have
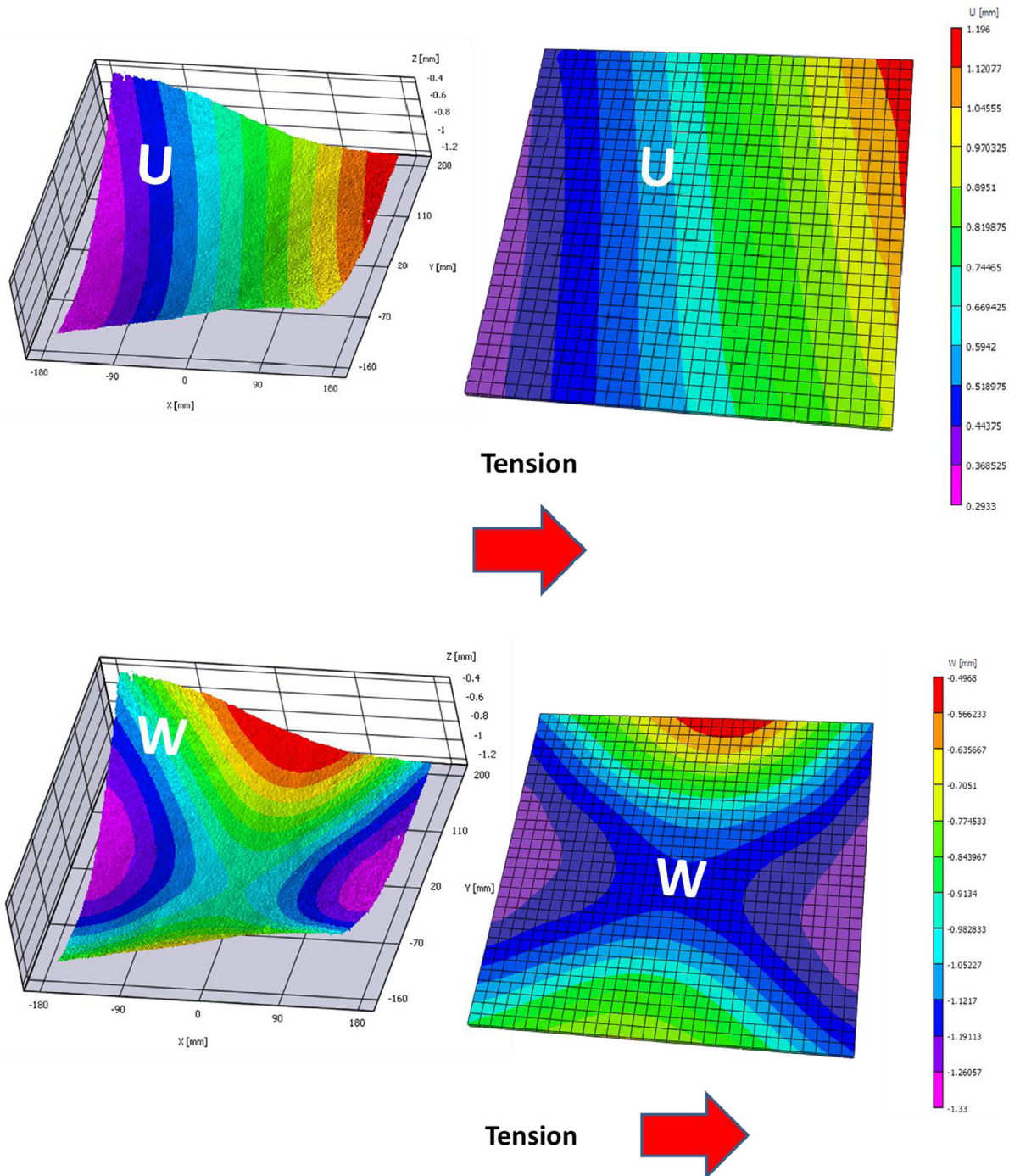

Fig. 26. Experimental (left) and numerical (right) in-plane displacement (U) and out-of-plane displacement (W) for maximum tension.
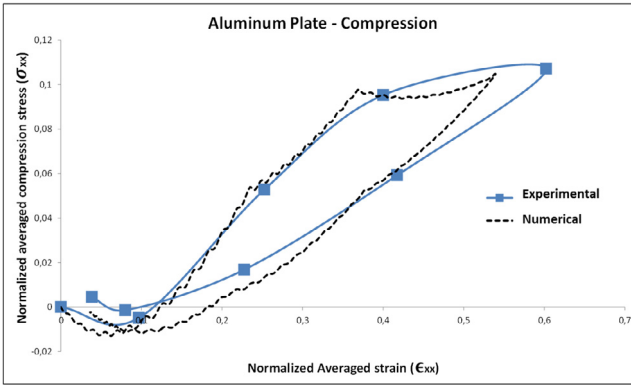
Fig. 27. Normalized averaged stresses vs normalized averaged strains for compression on aluminum plate.

to be compensated by displacement driving. In addition, the torsional loads inside the jacks were not the same for equal displacements. The phenomena may be related. A test was run by imposing load equality in the two jacks but the results were practically the same with, however, a slightly higher shear strain.

The failure pattern of the composite specimen is shown in Fig. 17. The specimen stacking was of the [10/4/4/2] type and there was a 100 mm long and 2 mm wide cut in the center, obtained by milling. Failure initiated from the central notch despite significant deterioration in the bolted area. Splits appeared before the end-point fall and were very visible to the naked eye. Therefore, this test validated the design of the composite test specimens that would be tested later. This design is presented in the second part of this paper. In particular, the absence of reinforcement plies was justified because the failure occurred near the notch and not in the fixings. Note that this design is specific to this issue and that such specificity will usually be the rule [35,36]. However, for safety reasons, following this test, it was decided to add aluminum reinforcements to pass a percentage of the loads through friction instead of using washers under the heads of the screws as seen in Fig. 17. Failure was explosive and very energetic for a force level

of the bending jacks of 118 kN (about 50% of the maximum load). It also led to a resonance mode of the columns supporting the bending actuators. For higher loads it will probably be necessary to reinforce these support columns.

4.2. Quality of tests

Only the tensile and shear tests will be presented in this part, both for the sake of conciseness and because they are the most significant. The output of the three strain gauges for the tensile test is given in Fig. 18.a. The shear strain ε_{xy} is found to be very low. The ε_{yy} strain corresponds to the Poisson effect. In addition, the measurements of the strains obtained by the VIC-3D© software with virtual gauges located at the position in question are compared with the values given by the gauges on the external face. They provide, for maximum loading: ε_{xx} = 2640 µstrains (for 2630 µstrains by strain gauges), ε_{yy} = −1060 µstrains (−1060 µstrains by strain gauges y), ε_{xy} = 10 µstrains (at 0 µstrain by strain gauges). It is thus observed that the strains are almost equal on the two faces of the plate, which shows that the assembly does not introduce parasitic bending and that the test takes place in a tensile state. The strain field ε_{xx} is visible in Fig. 19. The field is relatively homogeneous with low gradients in the central zone (<10%). Qualitatively, it can be estimated that the gradients are less than 20% on 80% of the plate. There are edge effects due to fasteners but these are limited in space and intensity.

In shear, the imposition of a null displacement of the bending actuators, and thus the high rigidity in this direction, prevents the plate from being deformed and generates significant tensile strains (Fig. 18.b), while, in the y direction, these strains remain low. However, the test is clearly performed in preponderant shear and the field of deformations ε_{xy} is little disturbed (Fig. 19); it corresponds qualitatively to the theoretical field presented in Fig. 6.

4.3. Calculation/test dialogue methodology

The path to achieving the numerical simulation of the behavior of composite notched plates has been progressive. The first step was to validate the methodology for measuring and transferring
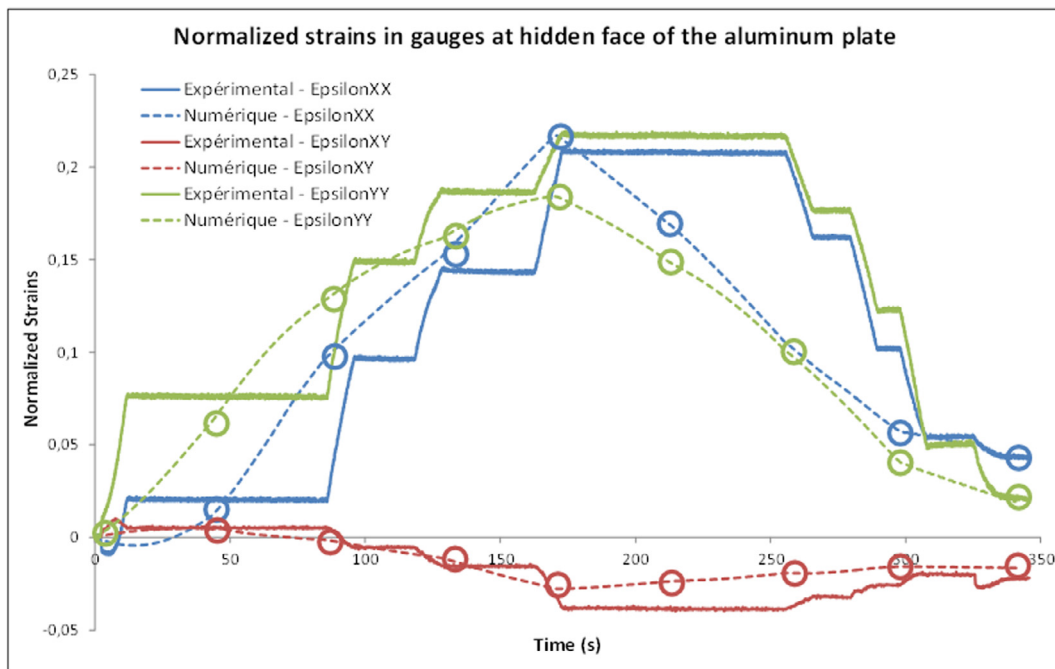

Fig. 28. Comparison of strains at the gauge locations for compression.

Maximum Compression

Experiment

Numerical results
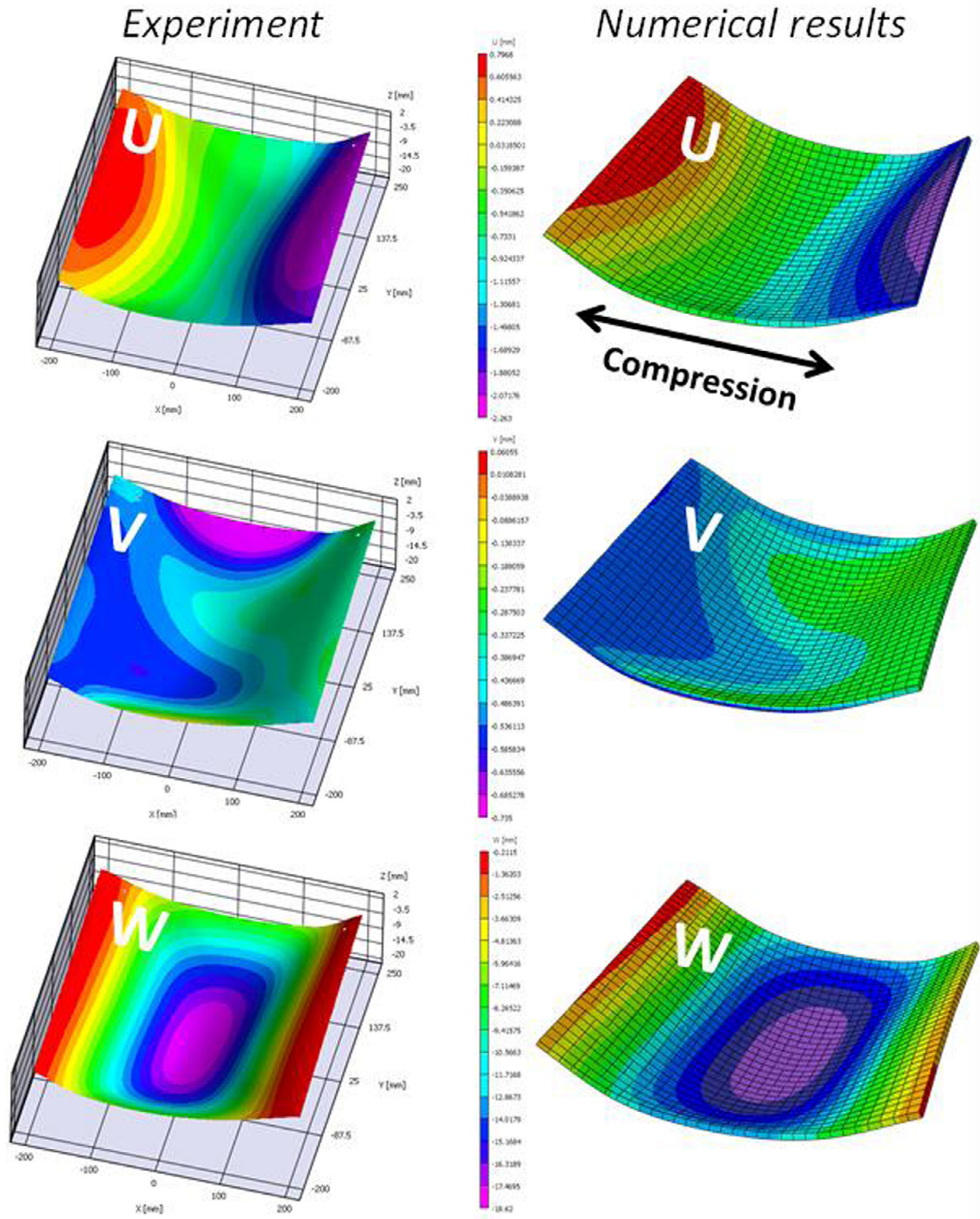
Fig. 29. Experimental (left) and numerical (right) in-plane displacement (U) and (V) and out-of-plane displacement (W) for maximum compression.

data on aluminum plates. A regular mesh of the plate was used (Fig. 20). The elements were thick shells (SC8 R) with dimensions $10 \times 10 \times 5$ mm^3 (only one element within the thickness). The elasto-plastic behavior law of aluminum is given in Fig. 21. The size of the elements was a compromise between the quality of the numerical approximation and the quality of the measurement by

Fig. 30. Normalized averaged stresses vs normalized averaged strains for shear on aluminum plate.
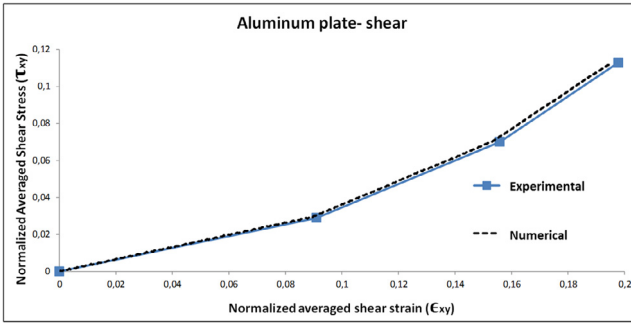
stereo correlation. The diagram presented in Fig. 20 shows the evolution of the various errors according to the size of the elements, the measurement by stereo correlation being based on an FE model [39]. The accuracy of a simulation using FE increases with the mesh density, that is to say, when the size of each element (h) decreases. The opposite trend is observed for stereo correlation measurements, which require at least 3 or 4 speckles per element in order to be able to determine the displacement fields, each speckle comprising several pixels. The model thus has 1024 elements and the calculation time associated with the different simulations is about 1 h using 4 CPUs.

The method for obtaining boundary conditions is inspired by the one developed by Sztefek and Olsson [44] (Fig. 22). The displacement field measurement is performed in Zone 1 (400×400 mm^2) which, in this study, has the advantage of being of constant thickness. The three displacements recovered by the FE-SDIC method are imposed on the edge of zone 1bis (red square, Fig. 22) and, in order to better simulate rotations, an out-of-plane displacement is imposed on 3 rows of additional nodes, (green area, Fig. 22). The useful zone (Zone 1bis), (used for the calculation by FE represented in Fig. 22), is smaller (320×320 mm^2) than the portion of the plate observed (Zone 1). This makes it possible to reduce the edge effects associated with stereo correlation measurement regularization (cf. Section 3). Numerically, the calculation is therefore divided into "n" steps of calculation

corresponding to the "n + 1" images provided by the stereo correlation cameras. A linear variation of the displacements is applied between the various states determined. An approximation of the loading (discretization in "n" segments of line) is therefore inherent in the proposed method. Three tests are presented here: tension, compression and shear.

4.3.1. Tension test

The imposition of boundary conditions on the edge of the mesh used (Fig. 22) generates a numerical edge effect: strains greater than those observed experimentally are noted on the first row of elements (Fig. 23). It is therefore necessary to select the area of calculation (of dimensions 20×300 mm^2) of the averaged stresses (Fig. 23). It is also noted that these two strips of elements at the edges of the specimen are the only ones that generate plastic strains; the remainder of the plate behaves linearly during this loading. This last remark will remain valid for the cases of compression and shear. After a calculation of the average stresses on these elements, it is possible to plot the experimental and numerical curves of the traction test (in "go/return"). These curves are shown in Fig. 24. The markers (blue squares) represent the experimental points associated with images taken by the stereo correlation cameras. The black circles on the numerical curve represent the corresponding states between which a linear approximation of the load is used. Very good agreement is observed between the experimental and numerical results despite the oscillations of the numerical curve due to the dynamic nature of the calculation (explicit solver). The values of the strains obtained by the numerical simulation, at the location where the gauges are placed, are very similar to the experimental values (Fig. 25). The deviations observed are related to the experimental method (increments of 10 mm in the displacement of the bending actuators n° 1 and 2 that are not simulated. It is also noted that the displacement fields U, V (not shown) and W, determined numerically, are close to those observed by stereo correlation, for the maximum tensile loading (Fig. 26), both quantitatively and qualitatively. The maximum deflections are very close.

4.3.2. Compression test

Using the same methodology, numerical and experimental stress/strain curves can be plotted (Fig. 27). They are very similar
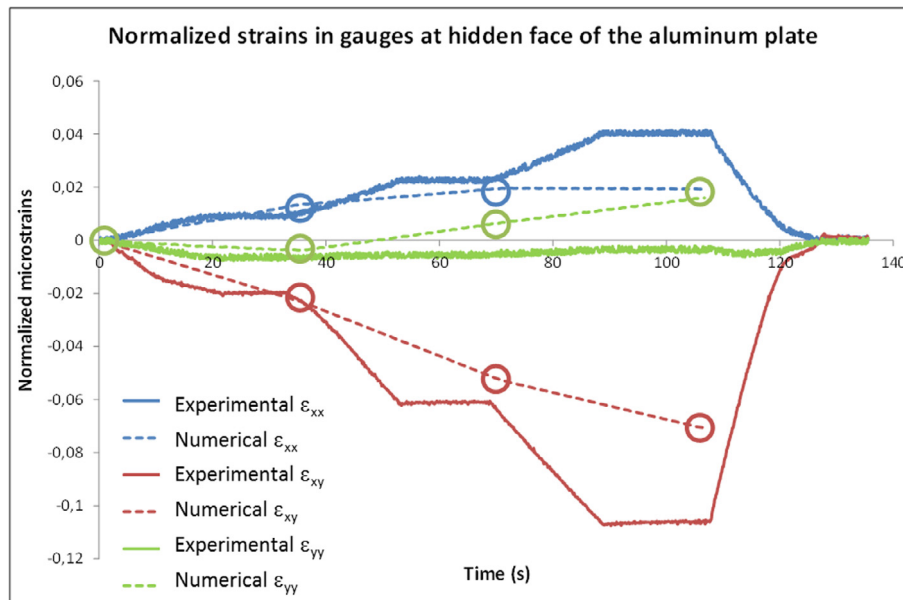

Fig. 31. Comparison of strains at the gauge locations for shear.

and evolve in the following way: the stress σ_{xx} is first negative and decreasing (simple compression) and then increases and even becomes positive. This is due to the global buckling phenomenon induced by the compression. Given the dimensions of the plate, buckling starts very early. It also has to be noted that the strains (ε_{xx} and ε_{yy}) measured on the bottom side of the aluminum plate (Fig. 28) are positive. In the zone of the gauges, the curvature is inverted with respect to the zone used for the calculation of the stresses at the edge of the plate. The double curvature generated by compression postbuckling is correctly captured by the numerical model. However, there are greater differences between the numerical and experimental values than in the case of tension
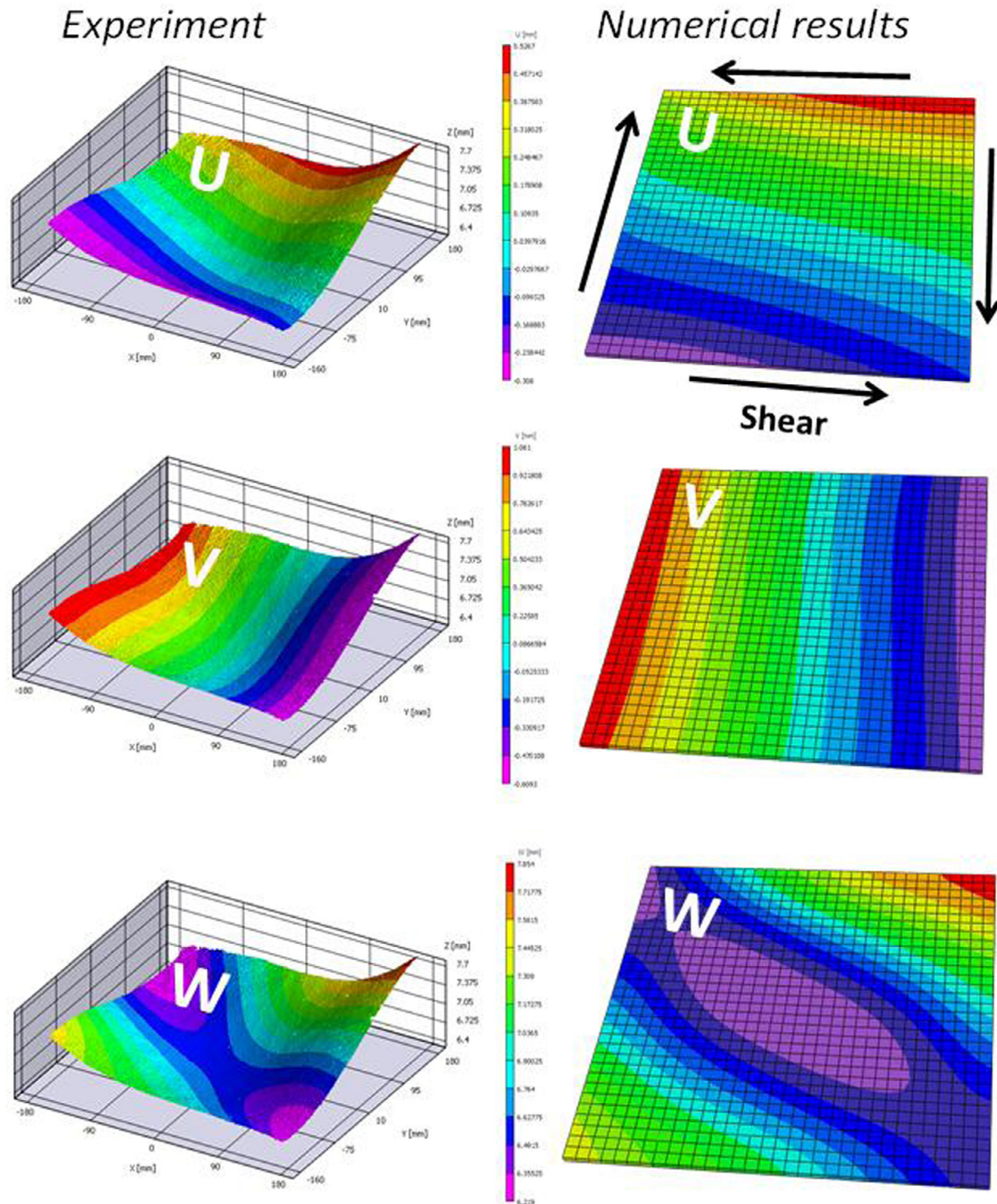

Fig. 32. Experimental (left) and numerical (right) in-plane displacement (U) and (V) and out-of-plane displacement (W) for maximum shear.

(Fig. 28). It is known that the buckling behavior is greatly affected by initial imperfections, which are not modeled in the numerical model, where the initial configuration is assumed to be perfectly plane. This may justify the discrepancies between the values obtained from the experimental and numerical strain gauges (Fig. 28). However, as for tension, numerical displacement fields very similar to those observed by stereo correlation are found at the maximum compression (Fig. 29).

4.3.3. Shear test

The strain/stress curves are obtained following the same method as the one described for tension and compression tests. Due to a manipulation error, the experimental and numerical curves were determined only up to the maximum shear value (Fig. 30). The stress/strain curve of the aluminum plate obtained numerically is very close to the one obtained experimentally. As for the local strain levels on the internal face (Fig. 31), shear-related strain/(ε_{xy}) is underestimated. At the maximum imposed shear loading, however, the numerically determined displacement fields are consistent with the experiment (Fig. 32), despite some differences in out-of-plane displacement (W). It should be noted that the deflection of the plate determined numerically (Fig. 32) corresponds to an expected shear buckling. The dissimilarities between the numerical simulation and the experimental data can thus also be attributed to the incorrect modeling of the initial imperfections. A second hypothesis could be that the measurement and transfer zone (zone 1 bis, Fig. 22) is insufficient to correctly account for a more complex distortion with more curvature change.

5. Conclusions

In this first paper, a methodology for testing composite structures under complex loadings is proposed. The development of a box type test rig is explained. The design ensures that the assembly can both transfer the highest loads and perform failure tests with strains of the order of 2%. Many practical problems such as driving the tests or mounting the plate have been solved. The structural tests are naturally more complex and a specific measurement procedure has been developed to overcome the specificity of the actual boundary conditions generated by the 128 bolts. The FE-SDIC method developed measures the initial shape and the displacement of the upper surface with a camera cluster in a frame, which is very suitable for the dialogue between tests and simulations. The use of multiresolution allows the spatial resolution of the measurement to be improved in regions of interest, and, in practice, permits direct use of the simulation mesh. The methodologies developed have been validated on isotropic plates and the quality of the tests has been demonstrated. The data exchange procedure between the FE-SDIC measurements and the non-linear Abaqus model made a global correlation possible with the experimental results. These methodologies can be further improved by using BC identified through the integrated FE-SDIC approach, and with better implementation of the initial conditions. For instance, by processing the images taken before and after the bolting procedure, it will also be possible to evaluate representative boundary conditions properly. This will enable the simulation to be as close as possible to the actual experimental conditions. In the second part of this publication, we will apply the methodology to the problem of large cuts in aeronautical composite structures.

Acknowledgements

References

[1] Rouchon J. Certification of Large Airplane Composite Structures, Recent Progress and New Trends in Compliance Philosophy. ICAS 1990;2:1439–47.
[2] Tropis A, Thomas M, Bounie JL, Lafon P. Certification of the composite outer wing of ATR 72. Proc Institu Mech Eng 1994;209:327–39.
[3] http://www.institut-clement-ader.org/vertex/.
[4] Abisset E, Daghia F, Ladevèze P. On the validation of a damage mesomodel for laminated composites by means of open-hole tensile tests on quasi-isotropic laminates. Comp Part A 2011;42(10):1515–24.
[5] Marcin L, Maire JF, Carrère N, Martin E. Development of a macroscopic damage model for woven ceramic matrix composites. Int J Dam Mech 2011;20 (6):939–57.
[6] Laurin F, Carrere N, Huchette C, Maire JF. A multiscale hybrid approach for damage and final failure predictions of composite structures. J Comp Mater 2013;47(20–21):2713–47.
[7] Camanho PP, Maimí P, Dávila CG. Prediction of size effects in notched laminates using continuum damage mechanics. Comp Sci Technol 2007;67 (13):2715–27.
[8] Chen JF, Morozov EV, Shankar K. A combined elastoplastic damage model for progressive failure analysis of composite materials and structures. Comp Struct 2012;94:3478–89.
[9] Bouvet C, Castanié B, Bizeul M, Barrau JJ. Low velocity impact modelling in laminate composite panels with discrete interface elements. Int J Sol Struct 2009;46(14–15):2809–21.
[10] Rivallant S, Bouvet C, Hongkarnjanakul N. Failure analysis of CFRP laminates subjected to compression after impact: FE simulation using discrete interface elements. Comp Part A 2013;55:83–93.
[11] Adam L, Bouvet C, Castanié B, Daidié A, Bonhomme E. Discrete ply model of circular pull-through test of fasteners in laminates. Comp Struct 2012;94 (10):3082–91.
[12] Achard V, Bouvet C, Castanié B, Chirol C. Discrete ply modelling of open hole tensile tests. Compos Struct 2014;113:369–81.
[13] Serra J, Bouvet C, Castanié B, Petiot C. Scaling effect in notched composites: the Discrete Ply Model approach. Comp Struct 2016;148:127–43.
[14] Van der Meer F, Sluys LJ. Mesh-independent modeling of both distributed and discrete matrix cracking in interaction with delamination in composites. Eng Fract Mech 2010;77(4):719–35.
[15] Van der Meer F, Sluys LJ, Hallett SR, Wisnom MR. Computational modeling of complex failure mechanisms in laminates. J Comp Mater 2012;46(5):603–23.
[16] Van der Meer FP, Davila CG. Cohesive modeling of transverse cracking in laminates under in-plane loading with a single layer of elements per ply. Int J Sol Struct 2013;50(20–21):3308–18.
[17] Iarve EV, Gurvich MR, Mollenhauer D, Dávila CG. Mesh independent matrix cracking and delamination modeling in laminated composites Int. J Num Meth Eng 2011;88(8):749–73.
[18] Chen BY, Tay TE, Pinho ST, Tan VBC. Modelling the tensile failure of composites with the floating node method. Comp Meth Appl Mech Eng 2016;308:414–42.
[19] Diyaroglu C, Oterkus E, Madenci E, Rabczuk T, Siddiq A. Peridynamic modeling of composite laminates under explosive loading. Comp Struct 2016;144:14–23.
[20] Hu YL, De Carvalho NV, Madenci E. Peridynamic modeling of delamination growth in composite laminates. Comp Struct 2015;132:610–20.
[21] Bertolini J, Castanié B, Barrau JJ, Navarro JP. Multi-level experimental and numerical analysis of composite stiffener debonding Part 2: element and panel level. Comp Struct 2009;90(10):392–403.
[22] Bisagni C, Vescovini R, Dávila CG. Single-stringer compression specimen for the assessment of damage tolerance of postbuckled structures. J. Aircraft 2011;48(2):495–502.
[23] Bisagni C, Dávila CG. Experimental investigation of the postbuckling response and collapse of a single-stringer specimen. Comp Struct 2014;108:493–503.
[24] Olsson R. A survey of test methods for multiaxial and out-of-plane strength of composite laminates. Comp. Sci. Tech. 2011;71:773–83.
[25] Wolf K, Kossira H. An Efficient Test Method for the Experimental Investigation of the Post-buckling Behavior of Curved Shear Panels. Amsterdam: ECCM Composite Testing and Standardization; 1992.
[26] Romeo G, Frulla G. Buckling and Post-buckling Behavior of Anisotropic Plates Under Combined Biaxial Compression and Shear Loads. Amsterdam: ECCM Composite Testing and Standardization; 1992.
[27] https://technologygateway.nasa.gov/docs/GFTD_V14k1.pdf.
[28] Lightfood MC, Ambur DR. Open Architecture data System for NASA Langley Combined Loads Test System. AIAA Paper AIAA-98-0345.
[29] Rouse M, Young RD, Ralph E. Gehrki RE. Structural Stability of a Stiffened Aluminum Fuselage Panel Subjected to Combined Mechanical And Internal Pressure Loads. AIAA Paper 2003–1423.
[30] Rouse M, Young RD. Design and evaluation of composite fuselage panels subjected to combined loading conditions. J. Aircraft 2005;42(4):1037–45.

[31] Bergan A, Bakuckas JG, Lovejoy A, Jegley D, Linton K, Korkosz G, Awerbuch J, Tan TM. Full-Scale Test and Analysis of a PRSEUS Fuselage Panel to Assess Damage-Containment Features. 2011 Aircraft Airworthiness & Sustainment Conference, San Diego, California, April 18–21, 2011.

[32] Best R, Fleischer T, Götze M, Sachse M, Semsch M. A Test Concept For Future Aircraft Fuselage Panels. 25th ICAF Symposium – Rotterdam, 27–29 May 2009.

[33] Peters RW. Buckling tests of flat rectangular plates under combined shear and longitudinal compression. NACA Technical Note 1948;1750.

[34] Klein H, General About Buckling Tests With Thin-walled Shells, Rapport DLR-Mitt, 89–13.

[35] Castanié B, Barrau JJ, Jaouen JP. Theoretical and experimental analysis of asymmetric sandwich structures. Comp Struct 2002;55(3):295–306.

[36] Castanié B, Barrau JJ, Jaouen JP, Rivallant S. Combined shear/compression structural testing of asymmetric sandwich structures. Exp Mech 2004;44 (5):461–72.

[37] Castanié B, Aminanda Y, Bouvet C, Barrau JJ. Core crush criteria to determine the strength of sandwich composite structures subjected to compression after impact. Comp Struct 2008;86:243–50.

[38] Garcia D. D, Orteu JJ, Penazzi L. A Combined Temporal Tracking and Stereo-correlation Technique for Accurate Measurement of 3D Displacements: application to sheet metal forming. J. Mater. Proc. Technol. 2002;125–126:736–42.

[39] Pierré JE, Passieux JC, Périé JN. Finite Element Stereo Digital Image Correlation: framework and mechanical regularization. Exp Mech 2017;53(7):443–56.

[40] Pierré JE, Passieux JC, Périé JN, Bugarin F, Robert L. Unstructured Finite Element-based Digital Image Correlation with enhanced management of quadrature and lens distortions. Opt Lasers Eng 2016;77:44–53.

[41] Passieux JC, Bugarin F, David C, Périé JN, Robert L. Multiscale displacement field measurement using digital image correlation: application to the identification of elastic properties. Exp Mech 2015;55(1):121–37.

[42] Réthoré J. A fully integrated noise robust strategy for the identification of constitutive laws from digital images. Int J Num Meth Eng 2010;84(6):631–60.

[43] Leclerc H, Périé JN, Roux S, Hild F. Integrated digital image correlation for the identification of mechanical properties. Lect N Comp Sci 2009;5496:161–71.

[44] Sztefek P, Olsson R. Tensile stiffness distribution in impacted composite laminates determined by an inverse method. Comp Part A 2008;39(8):1282–93.